Convolutional Neural Network Aided Chemical Species Tomography for Dynamic Temperature Imaging

Yalei Fu
School of Engineering
The University of Edinburgh
Edinburgh, UK
Y.Fu-28@sms.ed.ac.uk

Rui Zhang
School of Engineering
The University of Edinburgh
Edinburgh, UK
Renata.Zhang@ed.ac.uk

Godwin Enemali
School of Engineering
The University of Edinburgh
Edinburgh, UK
G.Enemali@ed.ac.uk

Abhishek Upadhyay
Department of Electronic and Electrical Engineering
The University of Strathclyde
Glasgow, UK
abhishek.upadhyay@strath.ac.uk

Michael Lengden
Department of Electronic and Electrical Engineering
The University of Strathclyde
Glasgow, UK
michael.lengden@strath.ac.uk

Chang Liu
School of Engineering
The University of Edinburgh
Edinburgh, UK
c.liu@ed.ac.uk

***Abstract*— Chemical Species Tomography (CST) using Tunable Diode Laser Absorption Spectroscopy (TDLAS) is an in-situ technique to reconstruct the two-dimensional temperature distributions in combustion diagnosis. However, limited by the lack of projection data, traditionally computational tomographic algorithms are inherently rank-deficient, causing artefacts and severe uncertainty in the retrieved images. Recently, data-driven approaches, such as deep learning algorithms, have been validated to be more accurate and stable for CST. However, most attempts modelled the phantoms using two-dimensional Gaussian profiles to construct the training set, enabling reconstruction of only simple and static temperature fields and can seldom retrieve the dynamic and instantaneous temperature imaging. To address this problem, we use Fire Dynamics Simulator (FDS) to simulate the dynamic and fire-driven reacting flows for training set construction. Based on this training set, a Convolutional Neural Network (CNN) is designed. This newly introduced method is validated by numerical simulation, indicating good accuracy and sensitivity in monitoring dynamic flames.**

***Keywords*—Dynamic, temperature imaging, Convolutional Neural Network (CNN), Tunable Diode Laser Absorption Spectroscopy (TDLAS), Chemical Species Tomography**

I. INTRODUCTION

By solving the inversion of the line-of-sight and sparsely-resolved Tunable Diode Laser Absorption Spectroscopy (TDLAS) measurements, Chemical Species Tomography (CST) has been developed as a powerful tool to quantitatively image the two-dimensional (2D) cross-sessional distributions of gas parameters, such as temperature [1], gas species concentrations [2], pressure [3] and velocity [4]. Concerning the influence of each parameter, effective inspection on the temperature is of significance as it strongly relates to the combustion process and directly determines gas composition within the combustion field [5]. A growing number of publications focus on exploring temperature imaging with high accuracy and reliability.

However, limited by the insufficient number of line-of-sight measurements, tomographic data inversion is inherently ill-posed and rank-deficient [6], which causes less accuracy and increased instability in the reconstructed images. Although various computational tomographic algorithms impose determined *a priori* for regularization [7-9], it is still challenging to eliminate the effects of artefacts. Instead of highly depending on the mathematical formulation, the deep learning technique provides an alternative approach to solve these ill-posed inverse problems [10].

Convolutional Neural Networks (CNNs) [11] have been applied to CST for reactive field prediction [12-15]. Although these innovative algorithms have been confirmed by both numerical simulation and lab-scale experiments, most of them are only available to reconstruct static and simple temperature distributions, as the training set is simulated by only considering simplified 2D profiles, e.g. Gaussian distributions. For a supervised deep learning method, the training set is the key factor to determine the performance of the model. These simple training samples are inadequate to represent the real scenarios in industrial applications.

Instead of reconstructing static temperature imaging where most studies are currently focusing on [14, 16, 17], the innovation of this proposed paper is the low-error reconstruction of dynamic flames. We integrate a computational fluid dynamics model into the generation of reacting flow fields. Being capable of describing flames in complex geometries and incorporating a wide variety of physical phenomena [18] in the training set, the proposed neural network is trained to extract the characteristics of dynamic and instantaneous temperature distributions. In addition, to get densely spatial samples, a tomographic sensor system with 128 laser beams from 4 equiangular views is constructed to build the forward absorption model.

II. METHODOLOGY

A. Mathematical formulation of CST

The formulation of CST is described in this section to enhance the understanding of the principles of image reconstruction.

When a laser beam at frequency ν [cm^{-1}] penetrates a sensing region filled with absorbing gas species with a path

This is a peer-reviewed, accepted author manuscript of the following conference paper:
Fu, Y. et. al., (2022). Convolutional neural network aided chemical species tomography for dynamic temperature imaging.
In 2022 IEEE International Instrumentation and Measurement Technology Conference (I2MTC). IEEE. https://doi.org/10.1109/i2mtc48687.2022.9806699

length L [cm], the intensity of the incident laser signal will be partially absorbed. Followed by Beer-Lambert relationship [19], the wavelength-dependent absorbance can be expressed as

$$\alpha(\nu) = \ln\frac{I_0(\nu)}{I_t(\nu)} = \int_0^L P(l)X(l)S\big(T(l)\big)\phi(\nu,l)dl, \quad (1)$$

where $I_0(\nu)$ and $I_t(\nu)$ are the incident and transmitted laser intensities, respectively. $P(l)$ [atm] is the local pressure and $X(l)$ denotes the molar fraction of targeted (absorbing) gas species. $S(\cdot)$ [cm^{-2}atm^{-1}] is the temperature-dependent line strength. $T(l)$ [K] is the local temperature. $\phi(\cdot)$ [cm] is the lineshape function.

Because the lineshape function $\phi(\cdot)$ is normalized thus it can be integrated as $\int_{-\infty}^{+\infty}\phi(\nu,l)d\nu = 1$. The path-integral absorption A_ν of this transition, which is also defined as the area underneath this lineshape function, can be described as

$$A_\nu = \int_{-\infty}^{+\infty}\alpha_\nu d\nu = \int_0^L [P(l)\cdot S(T)\cdot X(l)]dl = \int_0^L \alpha_\nu(l)dl, \quad (2)$$

where α_ν is the local absorbance density of the path integral.

For CST, the sensing region is discretized into J pixels, as shown in Fig. 1. In each pixel, temperature T, gas concentration X, as well as pressure P are assumed to be constant. Therefore, Equation (2) can be simplified as

$$\boldsymbol{A}_\nu = \boldsymbol{L}\boldsymbol{\alpha}_\nu, \quad (3)$$

where $\boldsymbol{A}_\nu$ is the vector of path-integral absorption obtained from TDLAS measurements and its element $\boldsymbol{A}_{\nu,i}$ represents the path-integral absorption of the i-th laser beam. $\boldsymbol{L} \in \mathbb{R}^{I\times J}$ is the sensitivity matrix where its component $L_{i,j}$ denotes the length of laser path segment of i-th laser beam within j-th pixel. $i \in \{1, 2,\ldots, I\}$ and $j \in \{1, 2,\ldots, J\}$ are the indices of the laser beams and pixels, respectively. $\boldsymbol{\alpha}_\nu \in \mathbb{R}^{J\times 1}$ is the vector of absorption density with its element $\alpha_{\nu,j} = P_j X_j S(T_j)$ for j-th pixel.

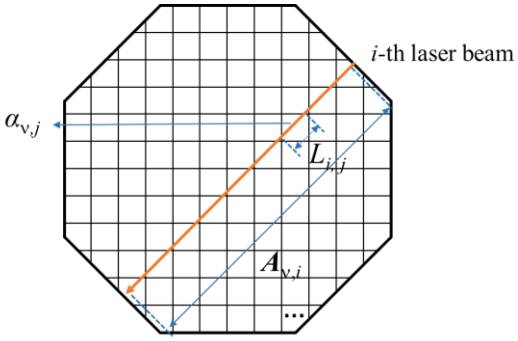

Fig. 1. The simplified numerical representation of the octagonal sensing region

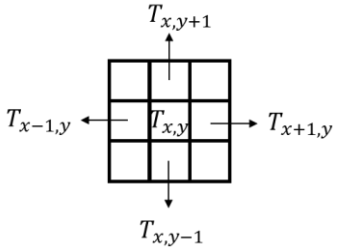

Fig. 2. One unit extracted from the pixelized sensing region

B. *Priori information*

Instead of training the proposed neural network that only relies on the dataset, some *a priori* information for the reconstruction of dynamic temperature is helpful to regularize and accelerate the process of model training.

In this work, two pieces of prior knowledge are imposed into the model to promote the learning ability of the CNN. First, the temperature is smoothly distributed. Regarding each local 9-pixel square in the sensing region as one unit, as shown in Fig. 2, the temperature in the central pixel $T_{x,y}$ obeys

$$\left| T_{x,y} - \frac{1}{4}\left(T_{x-1,y} + T_{x+1,y} + T_{x,y-1} + T_{x,y+1}\right)\right| < \theta, \quad (4)$$

where θ is the threshold.

Second, as the optical paths of the lasers from the same angular view are similar, the theoretical measurements of adjacent laser beams will represent strong smoothness and correlation. As CNN is trained on the basis of receptive field filtered by a kernel, reshaping the correlated laser measurements to align with the size of the kernel facilitates the extraction of smoothness features from absorption spectroscopic imaging.

C. *Model Architecture*

As shown in Fig. 3, the proposed CNN-aid model consists of two main parts: convolutional layers and fully-connected layers. By integrating the model with *a priori* information from smoothness, which has been mentioned before, the measurements $\boldsymbol{A}_{\nu_1} \in \mathbb{R}^{I\times 1}$ and $\boldsymbol{A}_{\nu_2} \in \mathbb{R}^{I\times 1}$ from two absorption transitions are reshaped to generate the input feature maps $\boldsymbol{C}_{\nu_1} \in \mathbb{R}^{H\times W}$ and $\boldsymbol{C}_{\nu_2} \in \mathbb{R}^{H\times W}$, respectively. Then, the stacked $\{\boldsymbol{C}_{\nu_1}, \boldsymbol{C}_{\nu_2}\}$ is constructed to find the mapping relationship to the unknown temperature vector $\boldsymbol{T} \in \mathbb{R}^{J\times 1}$. This model contains two convolutional layers Conv1 and Conv2, four fully-connected layers FC1, FC2, FC3 and FC4. The involved mathematical operations will be detailed as follows:

1) *Convolutional layers*

The convolutional layers can be mathematically expressed as

$$\boldsymbol{O} = \eta(\boldsymbol{W}*\boldsymbol{I} + \boldsymbol{b}), \quad (5)$$

where $\boldsymbol{I} \in \mathbb{R}^{H_I\times W_I\times C_I}$ is the input or intermediate feature maps, $\boldsymbol{O} \in \mathbb{R}^{H_O\times W_O\times C_O}$ the output feature map, $\boldsymbol{W} \in \mathbb{R}^{H_W\times W_W\times C_W}$ the kernel matrix, $\boldsymbol{b} \in \mathbb{R}^{C_b\times 1}$ the bias vector. $*$ is the operand for 2D convolution, $\eta(\cdot)$ the activation function. Furthermore, H_I (H_O), W_I (W_O) and C_I (C_O) are the height, width and the number of channels of $\boldsymbol{I}$ ($\boldsymbol{O}$). H_W, W_W and C_W are the filter height, filter width and the number of filters, respectively. C_b is the number of elements in b. The convolutional operation aims to extract the local connectivity of input feature maps so that the extracted characteristics can be further trained in the following fully-connected layers.

2) *Fully-connected layers*

The forward propagation within fully-connected layers can be described as

$$\boldsymbol{O} = g(\boldsymbol{W}\boldsymbol{I} + \boldsymbol{b}), \quad (6)$$

where $\boldsymbol{I} \in \mathbb{R}^{N_I\times 1}$, $\boldsymbol{O} \in \mathbb{R}^{N_O\times 1}$, $\boldsymbol{W} \in \mathbb{R}^{N_O\times N_I}$ and $\boldsymbol{b} \in \mathbb{R}^{N_O\times 1}$ are input vector, output vector, weight matrix and bias vector, respectively. $g(\cdot)$ represents the activation function. The fully-

connected layer provides a convenient way to learn the non-linear combinations of extracted features and to change the flatten vector to the desired dimension.

III. Model Training and Testing

A. Simulation Setup

To test the designed algorithm, the optical layout with 128 laser beams is first developed in this section. As shown in Fig. 4, 128 beams are divided into four groups and arranged in four equiangular projection angles at 0˚, 45˚, 90˚ and 135˚, each angle with 32 equispaced parallel beams. The distance between the adjacent beams is 0.63 cm, which makes the octagonal sensing region with a side length of 48.7 cm. To achieve high spatial resolution of the reconstructed gas image as well as considering the limited laser beams, this sensing region is determined to be uniformly discretized into 7,674 pixels. The central area with the densest beam arrangement, named Region of Interest (ROI), has 40 × 40 pixels with a side length of 20.2 cm. Water vapour (H_2O) is a significant product of combustion with strong near-infrared absorption spectrums. Hence it is chosen as the desired target absorption species to evaluate the performance of the proposed model. Two absorbing transitions at ν_1 = 7185.6 cm^{-1} and ν_2 = 7444.36 cm^{-1} are selected [20]. Along with the projection data from the 128-beam tomographic sensor, the measurements $\boldsymbol{A}_{\nu_1} \in \mathbb{R}^{128\times1}$ and $\boldsymbol{A}_{\nu_2} \in \mathbb{R}^{128\times1}$ will be obtained at ν_1 and ν_2, respectively. Table I shows the empirically determined hyper-parameters for model implementation.

B. Dataset Construction

Instead of simulating 2D distributions of temperature and species concentration by simple Gaussian profile, we use Fire Dynamics Simulator (FDS), which is developed by National Institute of Standards and Technology (NIST), to simulate heat transport of fire dynamics [21]. By solving a form of Navier-Stokes equations [22], FDS is capable of mimicking the temperature distributions within a dynamic field to the greatest extent. In this paper, a circular burner is modelled. To realize the reactive flow field of this burner model, we established an open 3D space with a 96 × 96 × 96 Cartesian mesh corresponding to 48.7 cm × 48.7 cm × 48.7 cm domain with open boundaries. The burner locates at the center of the lower boundary. Thus, a simple upwind boundary condition is built, which has little effect on the development of the burner within this computational domain [21]. Propane is chosen as the fuel. To improve the generalization of the model, the training set is established by simulating and recording the whole burning process.

After visualizing the output of FDS by Smokeview, the cross-sectional images of temperature and gas concentration at 6 cm above the burner outlet are saved with automatically adjusted time step, which obeys Courant-Friedrichs-Lewy condition [21]. The obtained dataset contains 11,714 samples from 10 different simulations by varying the mass fraction of the propane, flame duration and the spread rate of the flame. The sensitivity matrix $\boldsymbol{L}$ has been determined by the optical layout of the tomography system. Therefore, after generating the phantoms of 2D distributions of temperature and gas concentration, the path-integral absorption for each transition $\boldsymbol{A}_{\nu_1}$ and $\boldsymbol{A}_{\nu_2}$ can be calculated by following equation (2). It is then randomly divided into a training set with 11,125 samples and a test set with 589 samples.

Standardization can feature scaling to accelerate the convergence of the training process and improve the stability of the model. Thus, the simulated $\boldsymbol{A}_{\nu,i}$ is rescaled to $\boldsymbol{A}_{\nu}^{s}$ by:

$$\boldsymbol{A}_{\nu}^{s} = \frac{\boldsymbol{A}_{\nu,i} - \mu_{\boldsymbol{A}_{\nu,i}}}{\sigma_{\boldsymbol{A}_{\nu,i}}}, \tag{7}$$

where $\mu_{\boldsymbol{A}_{\nu,i}}$ is the mean value of the path-integrated absorption for i-th laser beam in the training set, $\sigma_{\boldsymbol{A}_{\nu,i}}$ the standard deviation. To align the test data with the trained model, $\boldsymbol{A}_{\nu,i}$ within the test set will follow the same calculation for rescaling. Finally, the stacked $\{\boldsymbol{A}_{\nu_1}^{s}, \boldsymbol{A}_{\nu_2}^{s}\}$ and corresponding temperature distribution $\boldsymbol{T} \in \mathbb{R}^{7674\times1}$ will be deployed into the model for training and testing.

TABLE I. Empirical-determined Hyper-parameters of the Model

	Layers			
Name of the layer	**Input dim.**	**Output dim.**	**Weight matrix**	**Stride**
Conv1	8 × 16 × 2	7 × 8 × 8	2 × 2	(1,2)
Conv2	7 × 8 × 8	6 × 7 × 32	2 × 2	(1,1)
FC1	1344	2048	--	--
FC2	2048	4096	--	--
FC3	4096	4096	--	--
FC4	4096	7674	--	--

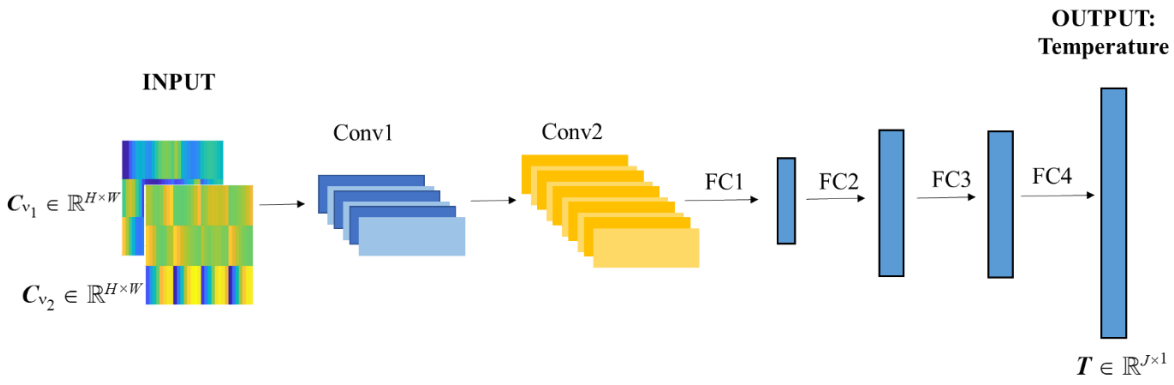

Fig. 3. The architecture of the established model.

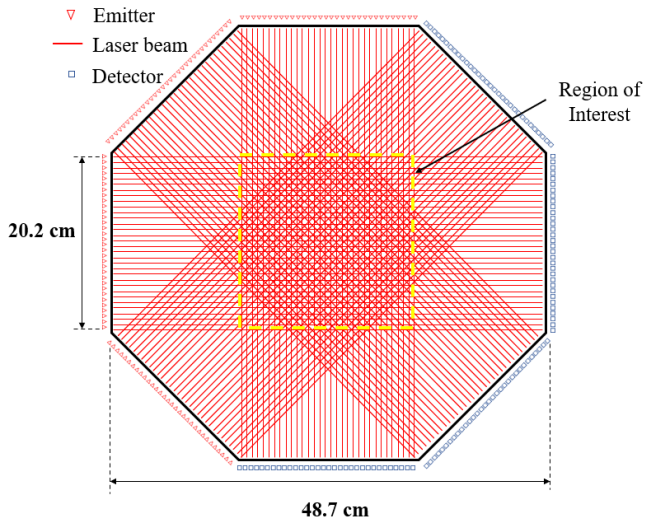

Fig. 4. The proposed beam arrangement for CST image reconstruction

C. Loss Function

The proposed algorithm is trained by a customized loss function after considering the *a priori* smoothness information, being demonstrated in session II. B, as well as the importance of temperature reconstruction in the ROI and the background. The loss function can be expressed as

$$\begin{aligned}\text{Total Loss} = \lambda \times \frac{1}{B}\sum_{b=1}^{B}\left\|\boldsymbol{T}_b^{rec,ROI} - \boldsymbol{T}_b^{tru,ROI}\right\|_2 + \\ \frac{1}{B}\sum_{b=1}^{B}\left\|\boldsymbol{T}_b^{rec,BG} - \boldsymbol{T}_b^{tru,BG}\right\|_2 + \\ \frac{1}{B}\sum_{b=1}^{B}\left\|T_b^{rec,ROI(x,y)} - T_b^{rec,smooth}\right\|_2,\end{aligned} \tag{8}$$

where B represents the batch size, equalling 128. $\boldsymbol{T}_b^{rec,ROI} \in \mathbb{R}^{1600\times 1}$ and $\boldsymbol{T}_b^{tru,ROI} \in \mathbb{R}^{1600\times 1}$ are the reconstructed and the true image vectors of b-th training sample within ROI, respectively. λ is a training-determined hyper-parameter, equalling 1.5. This term strengthens the reconstructed image error sourced from ROI. $\boldsymbol{T}_b^{rec,BG} \in \mathbb{R}^{6074\times 1}$ and $\boldsymbol{T}_b^{tru,BG} \in \mathbb{R}^{6074\times 1}$ are the reconstructed and the true image vectors of b-th training sample in the background, respectively. $T_b^{rec,smooth}$ equals to

$$\frac{1}{4}\left(T_b^{rec,ROI(x-1,y)} + T_b^{rec,ROI(x+1,y)} + T_b^{rec,ROI(x,y-1)} + T_b^{rec,ROI(x,y+1)}\right). \tag{9}$$

The third term of the loss function imposes smoothness regularization.

D. Other Training Details

ReLU is chosen as the activation function. L2 regularization is deployed into the loss function to avoid overfitting with a penalty factor 2×10^{-6}. Adam optimizer is implemented with a learning rate of 2×10^{-4}. The number of epochs is 400 to allow the model to fully converge in an NVIDIA Tesla P100 GPU on Google Colab.

E. Test Results

Besides the original test set, which is split from the FDS simulation dataset without additional noise contamination, three more test sets are generated to validate the proposed model in complicated dynamic flow fields by adding different levels of white noise on path-integral absorption, following this formulation:

$$\boldsymbol{A}_{n,i} = \boldsymbol{A}_{v,i} + n_{\boldsymbol{A}_{v,i}}, \tag{10}$$

where $\boldsymbol{A}_{n,i}$ is the contaminated path-integral absorption of i-th beam and $n_{\boldsymbol{A}_{v,i}}$ is the white noise. Then, four test sets with no noise, 20 dB noise, 30 dB noise and 40 dB noise are fed into the well-trained model, respectively. Image error (IE) evaluates the overall quality of the reconstructed image by considering each pixel's error, thus can represent the ability of the model on dynamic flow field retrieval. It is defined as

$$\text{IE} = \frac{1}{\text{Q}}\sum_{q=1}^{\text{Q}}\frac{\left\|\boldsymbol{T}_q^{rec} - \boldsymbol{T}_q^{tru}\right\|_2}{\left\|\boldsymbol{T}_q^{tru}\right\|_2}, \tag{11}$$

where Q and q are the total numbers of test samples and the sample index, respectively. $\boldsymbol{T}_q^{tru}$ and $\boldsymbol{T}_q^{rec}$ denote the temperature vectors of the ground truth and the reconstruction for q-th test sample, respectively. $\|\cdot\|_2$ is a Euclidean norm of the vector.

Fig. 5 depicts the dependency of IEs on different noise levels for the optimally trained model. It can be seen obviously that IE decreases as SNR increases. More specifically, IEs remain the small values and increase only by 0.5% when SNR varies from 0 to 20 dB. It indicates the reliability and robustness of the proposed algorithm in terms of strong noise tolerance and good accuracy for dynamic flow field reconstruction.

Regarding the practical SNR of 30 dB in physical experimental situations, the reconstructed results of the two selected phantoms from the test set with 30 dB noise are visualized in Fig. 6. In the first column, phantom (a) and (c) are the original temperature distributions, whereas phantom (b) and (d) in the second column are the corresponding reconstructions. Although it introduces much more complexity to the training model when trying to reconstruct dynamic flames, the proposed network can indicate the edge of the heat zone and specify the correct position of the peak temperature. In addition, the proposed algorithm eliminates image artefacts effectively. As a result, the reconstructed temperature images have better spatial resolution and accuracy.

IV. Conclusion

In this paper, an FDS-CNN hybrid algorithm is proposed to achieve dynamic temperature imaging. Coupled with the application of FDS, a mid-fidelity tool for reactive flow simulation, a circular burner is modelled and a training set is built by recording its whole combustion process. This new development captures dynamic features of the flame and builds an end-to-end mapping between the forward laser absorption and its temperature distribution. It reliably predicts each working state of the burner with fewer artefacts and higher image resolution, under the condition of limited projection data.

Quantified by IE in a wide range of SNRs, it is proved that this algorithm can effectively and stably capture the physical features from absorption data and have strong tolerance with noise-contaminated data. In summary, this physics-involved CNN-aid model investigates the dynamic evolution of the flames and reconstructs temperature imaging with good accuracy and robustness. In the future, it will be further

verified by experiment data and enhanced by incorporating temporal information for the prediction of gas parameters.

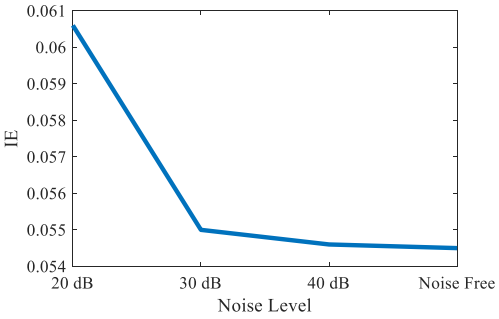

Fig. 5. The change of IEs when reconstructing the dynamic gas temperature images with different SNRs

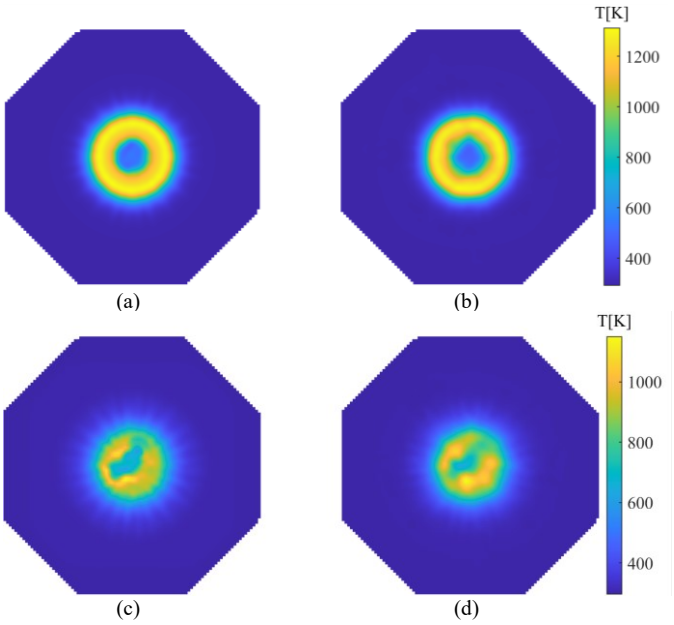

Fig. 6. Reconstruction of dynamic temperature images for the simulated circular burner phantoms when SNR is 30 dB. Phantom (a) and (c) are the ground-truth images from different time steps. (b) and (d) show the corresponding reconstructed temperature images.

ACKNOWLEDGMENT

The authors are grateful for financial support from the EPSRC Platform Grant EP/P001661/1.

REFERENCES

[1] C. S. Goldenstein, R. M. Spearrin, J. B. Jeffries, and R. K. Hanson, "Infrared laser-absorption sensing for combustion gases," Progress in Energy and Combustion Science, vol. 60, pp. 132-176, 2017.

[2] C. Liu, Z. Cao, Y. Lin, L. Xu, and H. McCann, "Online Cross-Sectional Monitoring of a Swirling Flame Using TDLAS Tomography," IEEE Transactions on Instrumentation and Measurement, vol. PP, no. 99, pp. 1-11, 2018.

[3] M. P. Wood and K. B. Ozanyan, "Simultaneous Temperature, Concentration, and Pressure Imaging of Water Vapor in a Turbine Engine," IEEE Sensors Journal, vol. 15, no. 1, pp. 545-551, 2015

[4] Q. Qu, Z. Cao, L. Xu, C. Liu, L. Chang, and H. McCann, "Reconstruction of two-dimensional velocity distribution in scramjet by laser absorption spectroscopy tomography," Applied optics, vol. 58, no. 1, pp. 205-212, 2019.

[5] H. Xia et al., "Two-step tomographic reconstructions of temperature and species concentration in a flame based on laser absorption measurements with a rotation platform," Optics and Lasers in Engineering, vol. 90, pp. 10-18, 2017.

[6] K. J. Daun, S. J. Grauer, and P. J. Hadwin, "Chemical species tomography of turbulent flows: Discrete ill-posed and rank deficient problems and the use of prior information," Journal of Quantitative Spectroscopy and Radiative Transfer, vol. 172, pp. 58-74, 2016.

[7] K. Daun, "Infrared species limited data tomography through Tikhonov reconstruction," Journal of Quantitative Spectroscopy and Radiative Transfer, vol. 111, no. 1, pp. 105-115, 2010.

[8] Y. Bao et al., "Relative entropy regularized TDLAS tomography for robust temperature imaging," IEEE Transactions on Instrumentation and Measurement, vol. 70, pp. 1-9, 2020.

[9] J. Dai, T. Yu, L. Xu, and W. Cai, "On the regularization for nonlinear tomographic absorption spectroscopy," Journal of Quantitative Spectroscopy and Radiative Transfer, vol. 206, pp. 233-241, 2018.

[10] C. Wei, K. K. Schwarm, D. I. Pineda, and R. M. Spearrin, "Physics-trained neural network for sparse-view volumetric laser absorption imaging of species and temperature in reacting flows," Optics Express, vol. 29, no. 14, pp. 22553-22566, 2021.

[11] Y. LeCun, Y. Bengio, and G. Hinton, "Deep learning," nature, vol. 521, no. 7553, pp. 436-444, 2015.

[12] C. Wei, K. K. Schwarm, D. I. Pineda, and R. M. Spearrin, "Deep neural network inversion for 3D laser absorption imaging of methane in reacting flows," Optics letters, vol. 45, no. 8, pp. 2447-2450, 2020.

[13] J. Huang, H. Liu, and W. Cai, "Online in situ prediction of 3-D flame evolution from its history 2-D projections via deep learning," Journal of Fluid Mechanics, vol. 875, 2019.

[14] Y. Jiang et al., "CSTNet: a dual-branch convolutional network for imaging of reactive flows using chemical species tomography," arXiv preprint arXiv:2010.03868, 2020.

[15] J. Huang, H. Liu, J. Dai, and W. Cai, "Reconstruction for limited-data nonlinear tomographic absorption spectroscopy via deep learning," Journal of Quantitative Spectroscopy and Radiative Transfer, vol. 218, pp. 187-193, 2018.

[16] J. Huang, J. Zhao, and W. Cai, "Compressing convolutional neural networks using POD for the reconstruction of nonlinear tomographic absorption spectroscopy," Computer Physics Communications, vol. 241, pp. 33-39, 2019.

[17] J. Si, G. Fu, R. Zhang, and C. Liu, "A quality-hierarchical temperature imaging network for TDLAS tomography," in 2021 IEEE International Instrumentation and Measurement Technology Conference (I2MTC), pp. 1-5, 2021.

[18] N. Gourdain et al., "High performance parallel computing of flows in complex geometries: II. Applications," Computational Science & Discovery, vol. 2, no. 1, p. 015004, 2009.

[19] C. N. Banwell, "Fundamentals of molecular spectroscopy," 1972.

[20] C. Liu, L. Xu, Z. Cao, and H. McCann, "Reconstruction of axisymmetric temperature and gas concentration distributions by combining fan-beam TDLAS with onion-peeling deconvolution," IEEE Transactions on Instrumentation and Measurement, vol. 63, no. 12, pp. 3067-3075, 2014.

[21] K. B. McGrattan et al., Fire dynamics simulator--Technical reference guide. National Institute of Standards and Technology, Building and Fire Research, 2000.

[22] S. V. Patankar, Numerical heat transfer and fluid flow. CRC press, 2018.